Materials Advances

ROYAL SOCIETY OF CHEMISTRY

PAPER

View Article Online
View Journal | View Issue

Check for updates

Cite this: *Mater. Adv.*, 2026, 7, 2701

# Gamma irradiation-induced structural and defect modulation in β-$TeO_2$ thin films at different annealing temperatures

K. Chandra,[a] M. G. Mahesha,[a] N. Karunakara[b] and Pramoda Kumara Shetty *[a]

Received 10th December 2025,
Accepted 16th January 2026

DOI: 10.1039/d5ma01443c

rsc.li/materials-advances

$TeO_2$ thin films were deposited on glass substrates using thermal vacuum deposition with optimized deposition parameters. The deposited films were subsequently exposed to gamma irradiation at doses ranging from 0 to 200 Gy and systematically characterized to evaluate the dose-dependent changes in structural, optical, and electrical properties. A notable temperature-dependent response was observed after thermal annealing. The samples annealed at 350 °C exhibited progressive crystallinity degradation with increasing gamma dose, whereas the samples annealed at 400 °C demonstrated enhanced crystallinity. X-ray photoelectron spectroscopy (XPS) and field emission scanning electron microscopy (FESEM) analyses revealed significant oxygen depletion in the 400 °C annealed samples following gamma irradiation. Raman spectroscopy revealed a pronounced shift in the characteristic peak for the 400 °C annealed films irradiated at 200 Gy; conversely, the Raman peak was entirely absent in the 350 °C annealed sample at the same irradiation dose, corroborating the XRD observations. The optical band gap exhibited an inverse relationship with increasing gamma dose. Photoluminescence measurements indicated reduced emission intensity at higher doses, attributed to enhanced non-radiative recombination pathways. The modulation of the EPR signal intensity observed before and after gamma irradiation demonstrates that the concentration of paramagnetic defects varies systematically with radiation dose, highlighting $TeO_2$ thin films as promising candidates for precision EPR gamma dosimetry and real-time radiation sensing applications. Electrical characterization demonstrated a dose-dependent increase in the concentration of paramagnetic defects at 200 Gy, which acted as trap centres. The study establishes annealing temperature as a critical controlling parameter governing radiation–matter interactions in $TeO_2$ thin films. It directly correlates oxygen depletion and paramagnetic defect evolution with dose-dependent changes in structural, optical, and electrical properties. Furthermore, the investigation reveals $TeO_2$ thin films as tunable EPR-based gamma dosimeters, wherein defect concentration and signal intensity can be precisely engineered through controlled annealing and irradiation dose for high-precision radiation sensing applications.

## Introduction

Studies on the effects of ionising radiation on materials are vital across diverse fields, including industry, medicine, nuclear power, cosmology, and radiation safety. These investigations underpin critical applications such as medical diagnostics, agricultural soil fertilisation, plant nutrition, and food preservation.[1,2] Despite extensive prior research, a comprehensive understanding of gamma irradiation's impact on material properties and its lingering after-effects remains essential. Ravi Kumar *et al.*[2,3] studied the $Cu^{2+}$: $Li_2Al_2SiO_6$ and doped $Li_2O–Al_2O_3–SiO_2–Y_2O_3$ glasses for thermoluminescence and electronic properties under gamma irradiation for dosimetry applications. Mohamed Elsaf *et al.*[1] investigated the necessity of gamma radiation detection and radiation protection in reducing health risks. They reported on the ability of $B_2O_3–ZnO–BaO$ glass in gamma shielding. Jyothi Budida *et al.*[4] reported the importance of gamma shielding and explored the material properties of $LiF–La_2O_3–PbO–B_2O_3$ using gamma attenuation studies. The influence of gamma irradiation on the improvement of the material properties was studied by Jyoti budida *et al.*[5] using lithium fluoro lanthanum oxy lead borate glasses. Furthermore, Thumma J *et al.*[6] reported that $TiO_2$-enhanced phosphate glasses exhibit radiation shielding efficiency close to that of the standard materials used for radiation

---

[a] *Manipal Institute of Technology, Manipal Academy of Higher Education, Manipal, Karnataka, 576104, India*
[b] *The Centre for Application of Radioisotopes and Radiation Technology, Mangalore University, Mangalagangotri, Mangalore, 574 199, Karnataka, India. E-mail: pramod.shetty@manipal.edu*

shielding. Similar work was carried out by Sumalatha J *et al.*[7] with the $Cr_2O_3$-doped lithium lead borosilicate glasses.

Problem statement: the formation and evolution of radiation-induced defects in metal oxides under gamma irradiation directly influence their electrical, optical, and magnetic properties; however, the precise dose-dependent relationships governing these changes remain poorly defined. This knowledge gap hinders the development of reliable radiation-sensing technologies, particularly for emerging needs in low-dose dosimetry and gamma-ray detection.

Research gap: while numerous studies have examined the effects of gamma radiation on various materials, including prior work on $TeO_2$ thin films for dosimetry,[8,9] the systematic correlation between defect dynamics and sensing performance as a function of irradiation dose (*e.g.*, 20–200 Gy) lacks detailed exploration. Key characteristics such as structural stability, optical shifts, electrical conductivity, and defect states in thermally evaporated β-$TeO_2$ films remain underexplored, despite the material's promise due to its high refractive index, strong nonlinear optical response, high dielectric constant, excellent thermal stability, and wide band gap.[10,11] Among the three stable phases of $TeO_2$, β-$TeO_2$ is notable for its thermodynamic stability, wide band gap, and superior charge mobility, making it an ideal candidate for bridging this gap.

This study addresses these challenges by analysing the structural, optical, electrical, and defect characteristics of annealed, thermal vacuum-deposited $TeO_2$ thin films on glass substrates, irradiated with gamma doses from 20 Gy to 200 Gy.

## Experimental details

The $TeO_2$ thin films were deposited using a thermal vacuum deposition system operated at a base pressure of $1 \times 10^{-6}$ mbar. Approximately 150 mg of $TeO_2$ powder was loaded into a tantalum boat, which was resistively heated by gradually increasing the current at a rate of 10 A $min^{-1}$. When the current reached 70 A, making the boat red-hot, the shutter opened to initiate deposition. The deposition was continued for 6 minutes, during which the current was further increased and maintained at 120 A, corresponding to a white-glow condition, after which the shutter was closed. Throughout the deposition process, the substrate temperature was maintained at 150 °C to ensure good adhesion between the film and the substrate. To improve crystallinity and achieve a stable phase, the deposited films were subsequently annealed at 350 °C and 400 °C at a heating rate of 20 °C $min^{-1}$. $TeO_2$ samples were irradiated with gamma radiation using a $^{60}Co$ source with an average energy of 1.25 MeV and a 5 Gy $min^{-1}$ dose rate. Structural analysis includes XRD, using a Rigaku Miniflex 600 with a Nickel filter at room temperature, and the $2\theta$ value ranging from 20° to 80°. Morphology and elemental analyses were done using a scanning electron microscope (FESEM, Quanta FEG 250), with gold sputtering before measurement to improve conductivity, since the sample was less conductive. To analyse the variation of chemical nature and evolution of the defect state of the sample with gamma dose, X-ray photoelectron spectra (XPS) were obtained using a PHI 5000 Versa Probe III, IITR. Raman spectra were obtained using a LAB RAM HR spectrometer (Horiba, France) with an excitation wavelength of 325 nm, 25 mW, operated at room temperature.

Optical band gap variation with gamma irradiation dose was analysed using optical absorption data obtained from UV-visible spectroscopy. Measurements were performed with a Shimadzu UV-3600 UV-vis-NIR spectrophotometer operating in the wavelength range of 200–1200 nm. Photoluminescence (PL) studies were carried out to investigate the optical nature of the defect states induced by irradiation, employing a LABRAM HR spectrometer (Horiba, France) with an excitation wavelength of 350 nm. Defect characterisation was further supported by electron paramagnetic resonance (EPR) analysis. EPR spectra of each sample were recorded at room temperature to correlate with other room-temperature measurements. The data were acquired using a JEOL Model JES FA200 EPR spectrometer operating within the X-band frequency range (8.75–9.65 GHz), with a sensitivity of $7 \times 10^9$ spins per 0.1 mT and a resolution of 2.35 μT. The magnetic field was varied from 0 to 800 mT with a step size of 0.024 mT, maintaining the sample surface perpendicular to the applied magnetic field. EPR data fitting and *g*-value analysis were performed using the Easyspin toolbox (version 6.0.8) in MATLAB 2024b. The spectral simulations were executed *via* the easyfit function based on the pepper simulation module, employing a least-squares fitting (LSF) algorithm with the Levenberg–Marquardt method and offset baseline correction. The spin system was modelled with $S = 1/2$ and anisotropic parameters appropriate for $TeO_2$ defect analysis. The fitted spectra were subsequently redrawn and analysed using OriginPro software. Electrical characterisation, including current–voltage (*I*–*V*) measurements and Hall analyses, was conducted using a Keithley 2450 source meter to evaluate the electrical properties of the irradiated films.

## Results and discussion

### Structural and compositional analysis

**X-ray diffraction studies.** Annealed samples (at 350 °C and 400 °C) from the previous work were irradiated at different doses of gamma radiation up to a maximum of 200 Gy. The XRD peaks were indexed by comparing them with the standard diffraction data of β-$TeO_2$, as the phase of the annealed sample had been confirmed in a previous study.

Both samples showed the formation of major diffraction peaks at the (012) and (101) planes. The intensity was found to increase with the dose. There were several other peaks identified at higher gamma dose irradiation and listed in Fig. 1. Similar findings have been reported in previous studies at significantly higher irradiation doses.[12,13] These studies attributed the observed effects to irradiation-induced agglomeration, which promotes crystal growth along specific crystallographic planes, while simultaneously generating structural defects and lattice disorder in the material.

Parameters of XRD analysis, such as crystallite size, micro strain and dislocation density, were calculated using the Debye–Scherrer formula and are listed in Tables 1 and 2.

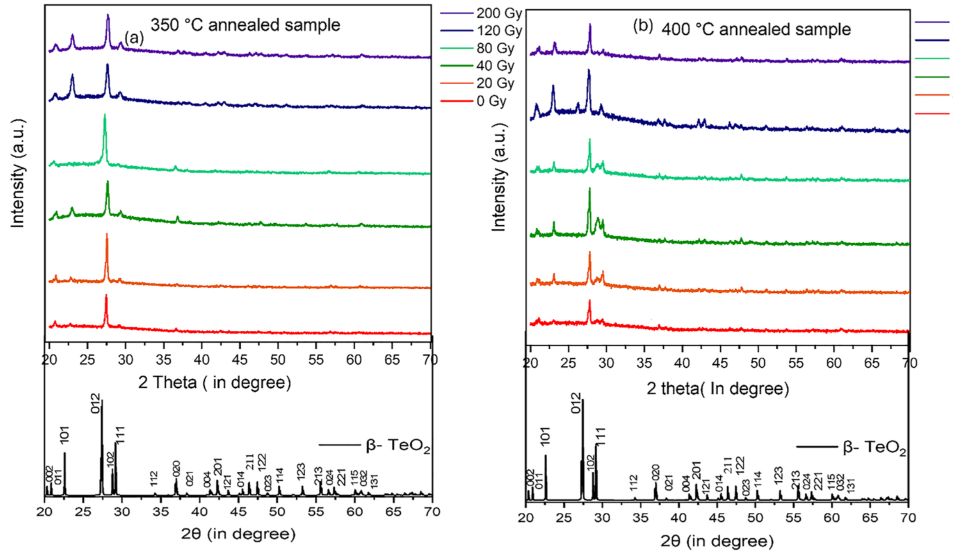

Fig. 1 XRD spectra of the irradiated sample at different gamma doses for (a) 350 °C and (b) 400 °C annealed samples, with their standard reflection plane for each angle.

Table 1 Structural parameters of the 350 °C annealed sample at different gamma doses

| Gamma dose (Gy) | Crystallite size ($D$) (nm) | Micro strain ($\varepsilon$) ($10^{-4)}$ | Dislocation density ($\delta$) ($10^{14}$)/m$^2$ |
|---|---|---|---|
| 0 | 41.3 ± 0.9 | 35.0 ± 0.7 | 5.9 ± 0.2 |
| 20 | 40.5 ± 0.7 | 36.0 ± 0.6 | 6.1 ± 0.2 |
| 40 | 33.2 ± 1.0 | 45.0 ± 1.3 | 9.0 ± 0.5 |
| 80 | 32.5 ± 0.7 | 45.0 ± 1.0 | 9.4 ± 0.4 |
| 120 | 28.0 ± 0.4 | 54.0 ± 0.7 | 12.8 ± 0.4 |
| 200 | 27.5 ± 0.5 | 55.0 ± 1.0 | 16.2 ± 0.6 |

Table 2 Structural parameters of the 400 °C annealed sample at different gamma doses

| Gamma dose (Gy) | Crystallite size ($D$) (nm) | Micro strain ($\varepsilon$) ($10^{-4}$) | Dislocation density ($\delta$) ($10^{14}$)/m$^2$ |
|---|---|---|---|
| 0 | 34.1 ± 3.0 | 43.0 ± 3.9 | 8.6 ± 0.8 |
| 40 | 42.1 ± 2.3 | 35.0 ± 1.8 | 5.6 ± 0.3 |
| 80 | 37.6 ± 4.4 | 39.0 ± 4.7 | 7.1 ± 0.9 |
| 100 | 35.9 ± 2.8 | 28.0 ± 2.0 | 3.7 ± 0.3 |
| 120 | 38.4 ± 1.3 | 50.0 ± 2.5 | 10.8 ± 0.3 |
| 200 | 50.0 ± 3.5 | 29.0 ± 2.0 | 4.0 ± 0.3 |

Of the two sample sets, the one annealed at 350 °C shows a decrease in crystallite size with the irradiation dose, within the uncertainty shown in Fig. 1(a). Gamma rays displace atoms from lattice sites, creating point defects (vacancies and interstitials) and disrupting long-range order, which broadens the XRD peaks and reduces the crystallite size. Hence, the decrease in crystallite size is directly correlated with defect formation. However, the other types of defects need to be analysed using further material characterisation. Microstrain and dislocation density are inversely proportional to crystallite size (Table 1).[14,15]

For the sample annealed at 400 °C (Fig. 1(b)), there was an increase in overall crystallite size with the increase in gamma dose (Table 2). The improvement in crystallinity with gamma irradiation at lower doses ranging from 0 Gy to 200 Gy was attributed to the local heating effect from lattice-phonon scattering, which alters the lattice parameters, crumbles grain boundaries and promotes defect per atom migration for larger grain coalescence. This releases strain locally between the film and the substrate and helps in the growth of crystallites.[13,16,17] The primary objective of understanding the role of annealing temperature in radiation–matter interactions was achieved through structural studies, which revealed contrasting crystallinity evolution in films annealed at 350 °C and 400 °C under identical gamma irradiation doses.

**FESEM analysis.** Field emission scanning electron microscopy (FESEM) and energy dispersive X-ray analysis (EDAX) were performed on the 400 °C annealed samples to examine the film morphology and compositional variations. The results, presented for both unirradiated (0 Gy) and irradiated (200 Gy) samples, reveal distinct changes upon gamma irradiation. The EDAX data indicate a reduction in oxygen concentration in the irradiated film, which can be attributed to oxygen desorption induced by gamma irradiation,[18,19] and also the sample annealed at 400 °C exhibited variation in the film morphology. It showed an irregular surface with larger fused structures and less distinct grain boundaries and less-defined structures compared to the unirradiated sample (Fig. 2(a) and (b)). Reduced oxygen (Table 3) interstitials may help in improving crystallinity and oxygen desorption leads to relaxation of the strain in the sample.

**XPS analysis.** Chemical composition-related studies of the sample after irradiation were carried out to analyse the effect of chemical composition on irradiation. The survey spectra of the 200 Gy irradiated 350 °C and the 200 Gy irradiated 400 °C annealed samples are shown in Fig. 3. For the 200 Gy irradiated 350 °C sample, the interstitial peak related to Te can be found in peak fitting, which was absent in the non-irradiated sample discussed before.[20] This suggests that irradiation causes

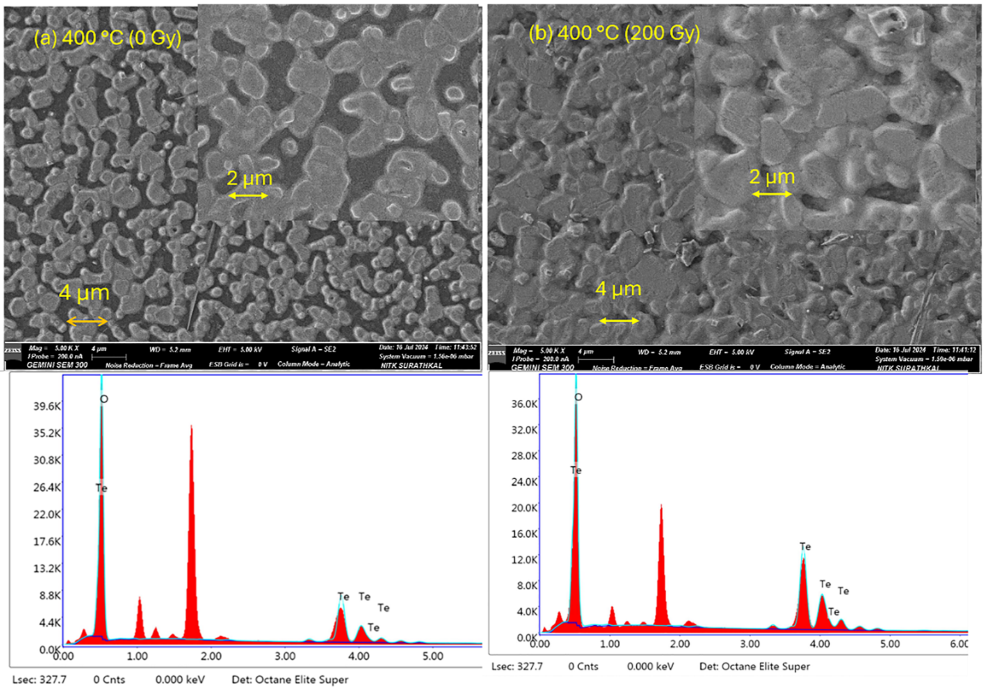

Fig. 2 FESEM images showing the morphology of the thin film before and after gamma irradiation, and the elemental analysis spectra for (a) 400 °C, 0 Gy and (b) 400 °C, 200 Gy. The inset figure shows the higher magnification image (2 μm).

Table 3 Elemental percentage of the samples before and after irradiation (at 200 Gy)

| | % of Te | | % of O | |
|---|---|---|---|---|
| Annealed sample | 0 Gy | 200 Gy | 0 Gy | 200 Gy |
| 400 °C | 24.20 | 38.96 | 85.80 | 61.04 |

displacement damage, leading to the formation of defects, and it was also evident that compared to the non-irradiated sample, the Te peaks (both Te $3d_{3/2}$ and Te $3d_{5/2}$) in the irradiated sample shifted towards higher binding energy by 0.6 eV (Fig. 4(a)). This is due to reduced crystallinity, which leads to a more delocalized electron distribution compared to crystalline materials, which have a well-defined atomic structure. In crystalline materials, the precise arrangement of atomic positions results in electrons being more localised around the atomic cores, whereas in less crystalline or amorphous materials, the lack of ordered structure causes the electrons to be more dispersed.[20,21] However, there was an improvement in crystallinity at 400 °C after irradiation.

The shift in B.E. (Fig. 4(b)) was attributed to a decrease in electron density around the nucleus, resulting from the electron-withdrawing effect. Vishnu Chauhan *et al.*[22] mentioned that a smaller shift in B.E. was due to radiolysis-related defects and damage. Additionally, Lee *et al.*[23] pointed out that the radiolysis process can generate reactive Te radicals near the surface, which interact with oxygen in a manner similar to the effect of $H_2O_2$

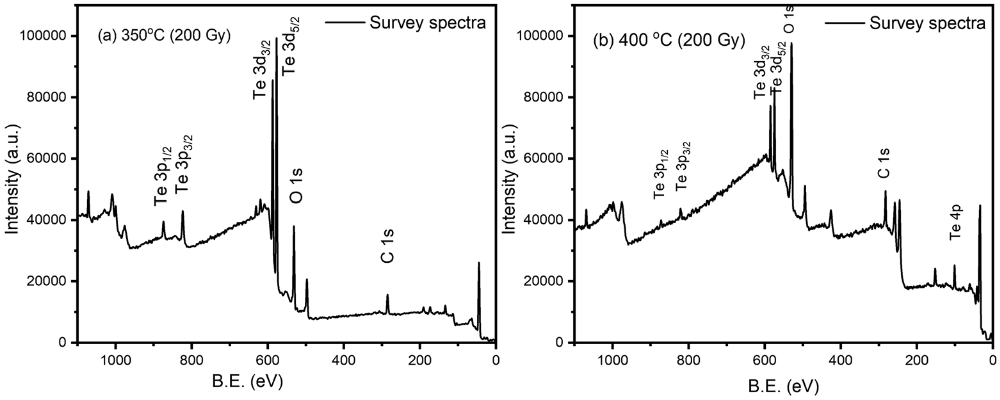

Fig. 3 XPS survey spectra of (a) 350 °C, 100 Gy and (b) 400 °C, 200 Gy samples.

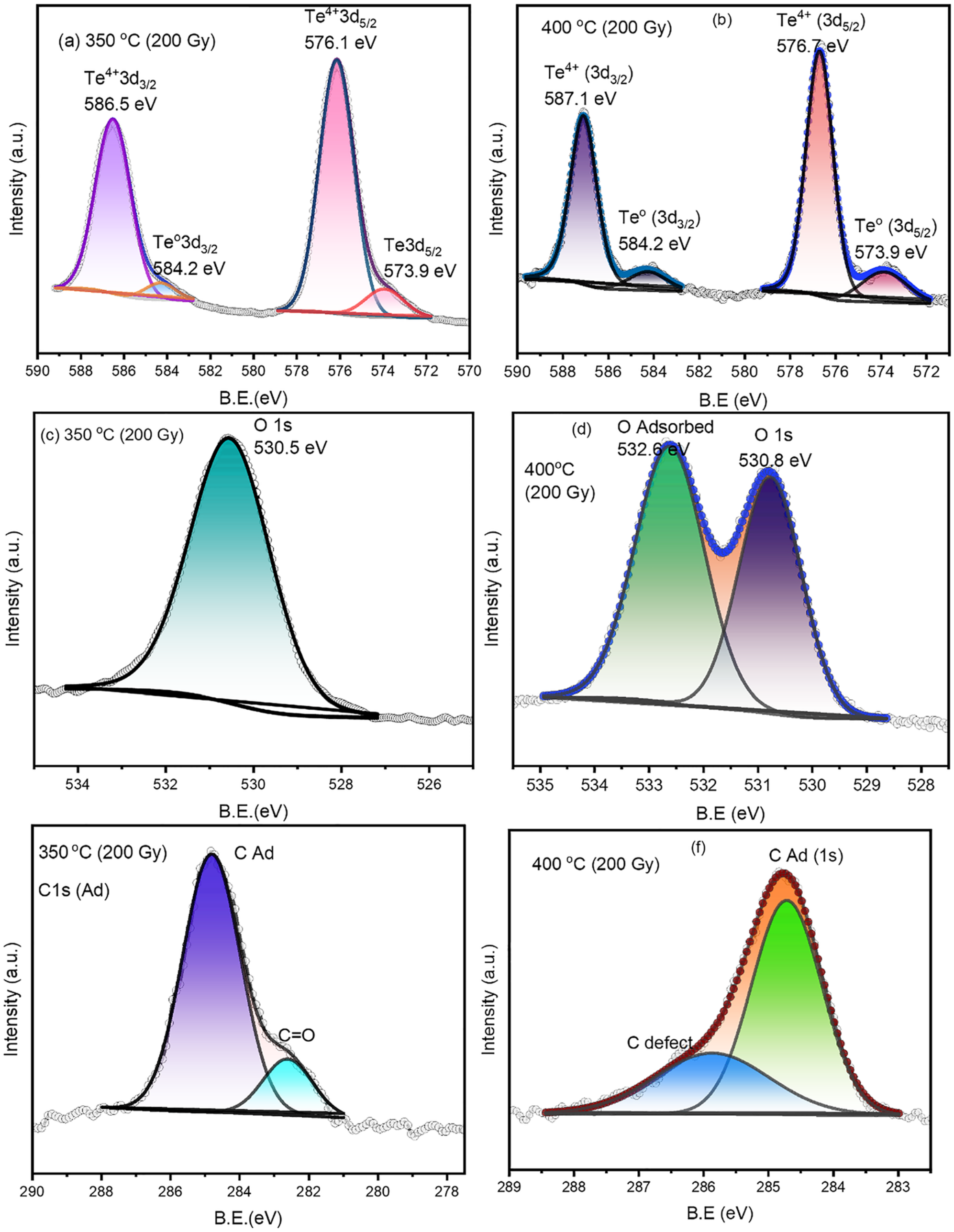

Fig. 4 XPS spectra and peak fitting of (a) Te 3d 350 °C, 100 Gy; (b) Te 3d 400 °C, 200 Gy; (c) O 1s, 350 °C, 100 Gy; (d) O 1s, 400 °C, 200 Gy; (e) C 1s, 350 °C, 100 Gy; and (f) C 1s, 400 °C, 200 Gy.

treatment on $TeO_2$. This interaction leads to a higher oxidation state of Te, specifically at the surface, resulting in a shift of the binding energy to higher values.[24] In contrast, bulk $TeO_2$ exhibits a more compact structure with fewer oxygen vacancies within the $TeO_2$ lattice. The additional peak observed at 573.9 eV for the Te $3d_{5/2}$ level, positioned at a higher binding energy compared to the elemental Te peak around 573 eV, can be attributed to tellurium present in interstitial sites or to chemical states associated with $TeO_2$-related transitions.

A single broad peak corresponding to O 1s (FWHM ~2 eV) matched with $O^{2-}$, indicating minimal traces of non-stoichiometric oxygen and adsorbed oxygen compared to lattice oxygen, which was difficult to deconvolute during peak fitting (Fig. 4(c)). However, the broadness of the peak suggests that the corresponding single peak also includes adsorbed and interstitial oxygen.

A similar trend for the 400 °C annealed and 200 Gy irradiated sample was observed in XPS analysis. The peak of lattice Te ($Te^{4+}$) at 576.7 eV ($3d_{5/2}$) and 587.1 eV ($3d_{3/2}$) shifted by 1.2 eV relative to the non-irradiated sample (Fig. 4). Since there was an increase in the peak corresponding to interstitial Te and also a decrease in oxygen concentration in EDS (Table 3), these shifts may relate to the defect environment around the lattice, which leads to a decrease in electron density and an increase in oxidation state. Gamma irradiation of metal oxide thin films commonly induces the formation of oxygen vacancies, leading to a reduction in oxygen concentration and corresponding modifications in the XPS O 1s spectra. The high-energy gamma photons displace oxygen atoms from their lattice sites, generating vacancy-related defects such as Frenkel or Schottky defects, which collectively contribute to a decrease in the overall oxygen content.

The oxygen peak consists of two almost equally intense peaks at 532.6 and 530.2 eV (Fig. 4(c) and (d)) and lies within the range of the O low binding energy peak (LP), mid binding energy peak (MP), and high binding energy peak (HP).[23,24] Here, LP corresponds to lattice oxygen ($O_L$), MP corresponds to oxygen deficiency, or vacancies ($O_o$), and HP corresponds to defects in interstitial and surface oxygen ($O_i$). Muhammad Abiyyu Kenichi *et al.*[25] reported B.E. of 529.6, 531.3, and 532.2 eV corresponding to lattice oxygen, oxygen vacancies or an oxygen deficient region and chemisorbed oxygen, respectively. Since EDS analysis shows a deficiency in O concentration for the 400 °C annealed and 200 Gy irradiated sample, 530.2 eV may correspond to $O_o$.[26]

The adventitious carbon (Ad C 1s) peak was found in all thin film XPS spectra at a B.E. of 284.8 eV.[27] XPS of Ad C 1s comprises two peaks, both in the 200 Gy (at 350 °C) and 200 Gy (at 400 °C) samples. But in the 200 Gy sample, the peak at the lower B.E. side was related to C=O.[28] In the 200 Gy irradiated sample, the peak in the higher B.E. region (282.6 eV) shifted nearly 1.2 eV from Ad C 1s (284.8 eV) (Fig. 4(e) and (f)), corresponding to the carbon defects.

**Raman analysis.** Raman spectra reveal the effect of irradiation on the sample by examining the variations in peak intensity, broadening (FWHM) and peak position. Raman spectra were analysed, and peaks were identified (listed in Table 4). All samples were β-$TeO_2$ (tellurite)[20] containing 24 atoms in a unit cell[29] and their vibration modes were given by the irreducible representation of the $D_{2h}$ point group as $\Gamma = 9A_g + 9B_{1g} + 9B_{2g} + 9B_{3g} + 9A_u + 8B_{1u} + 8B_{2u} + 8B_{3u}$ contains both Raman (g modes) and IR active modes ($B_u$-modes).[29,30] The modes 118 $cm^{-1}$ ($B_{2g}$), 139 $cm^{-1}$ ($B_{3g}$), 221 $cm^{-1}$ ($B_{1g}$) and 265 $cm^{-1}$ ($A_u$) were common to both nonirradiated[20] and irradiated samples annealed at 400 °C. These vibrational modes belong to the bulk $TeO_4$ polyhedra, which are common for both amorphous and crystalline $TeO_2$ and match with the other phases of $TeO_2$.

With the irradiation dose, peaks appear at the higher frequency Raman shift. Fig. 5 shows the Raman spectra of the 80 Gy and 200 Gy irradiated samples annealed at 400 °C. The higher frequency peaks were due to the intramolecular stretching and bending vibrations. One such mode was at ∼416 $cm^{-1}$ from the ring of $Te_2O_2$, which modulates the axial bond length,[31] and another peak at 675 $cm^{-1}$ originates from Te–O–Te, with motion of O along the equatorial line. These two peaks were specifically for the β-$TeO_2$ phase. Here, the intensity of the peak at 75 $cm^{-1}$ was slightly higher than that of the peak at 416 $cm^{-1}$, which arises from the asymmetry essential for the Te–O–Te linkage.[32] The wave number and the nature of the Raman vibrations are listed in Table 4.

Table 4 Raman shifts for different modes of vibration, along with their wavenumbers

| Raman shift ($cm^{-1}$) | Mode of vibration |
|---|---|
| ∼87 | Shift related to the bending and pulsation of $TeO_4$ polyhedra |
| ∼115 | |
| ∼136 | |
| ∼216 | |
| ∼264 | |
| ∼416 | $Te_2O_2$ length axis bond |
| ∼675 | Te–O–Te (motion of O along the equator.) |

Similarly, for the analysis of structural changes due to the gamma irradiation in the 350 °C annealed sample, the Raman data for the 80 Gy and 200 Gy dose irradiated samples are presented (Fig. 6). The results show that only the peak at a lower Raman shift indicates that radiation reduced crystallinity, unlike the 400 °C annealed sample. These results were correlated with XRD analysis. The presence of sharp Raman modes at higher wavenumbers, typically >600 $cm^{-1}$, corresponding to Te–O stretching bands, strongly indicates crystallinity in the $TeO_2$ thin films, as they arise from well-defined lattice vibrations in ordered structures. The peak at 518 $cm^{-1}$ arises for the 80 Gy irradiated sample, which was not found in the standard Raman spectra of $TeO_2$ for any other phase. But Champarnuad *et al.*[30] in their study reported that a peak may arise due to intra-sheet interaction in the layers of β-$TeO_2$. Morphological and chemical analyses confirmed oxygen depletion and defect generation, directly linking thermal treatment to radiation-induced structural stability. Raman spectroscopy further substantiated these findings by evidencing lattice distortion or amorphization consistent with the XRD results.

## Optical analysis

**UV visible spectroscopy study.** The variation of band gap and associated optical properties, such as absorbance and transmittance, with irradiation dose provides insights into the material's behaviour at different levels of gamma exposure. In general, band gap studies with respect to gamma irradiation dose help in understanding the formation of trap states and the behaviour of charge carriers within the forbidden energy gap.

The absorbance in the visible region and the NIR region decreased with irradiation dose except at 160 Gy for the 400 °C annealed sample (Fig. 7). Optical band gap $\left(E_g^\circ\right)$ variation is analysed using the Tauc plot. For the 400 °C annealed sample, $E_g^\circ$ increased with the dose value (Fig. 8) (Table 5). The enhancement of the optical band gap after irradiation arises from changes in the electronic structure and energy levels due to defect creation and increased carrier concentration. Aldawood *et al.*[33] discussed the effect of irradiation dose on the optical band gap $\left(E_g^\circ\right)$. They reported that changes in crystallinity post-irradiation, as observed in thin films, influence trap state densities within the CB and VB. For instance, gamma exposure reduced $E_g^\circ$ from defect-induced mid-gap states. Irradiation introduces defects that generate intermediate states

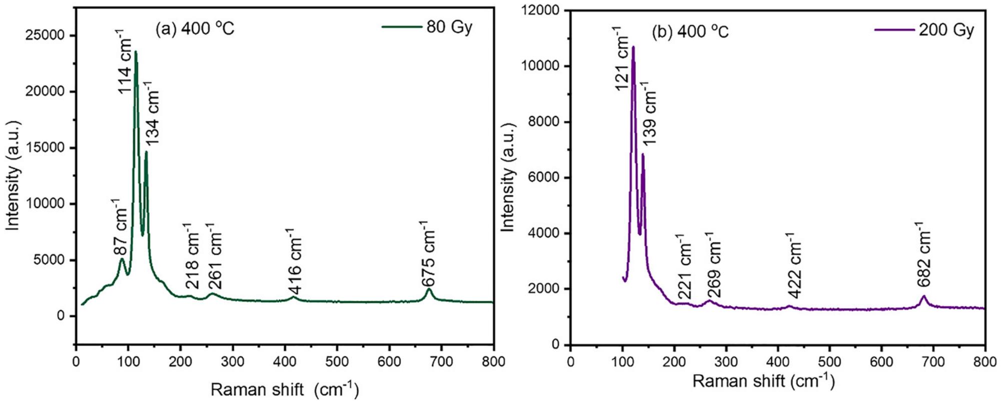

Fig. 5 Raman spectra of the 400 °C annealed sample at gamma doses (a) 80 Gy and (b) 200 Gy.

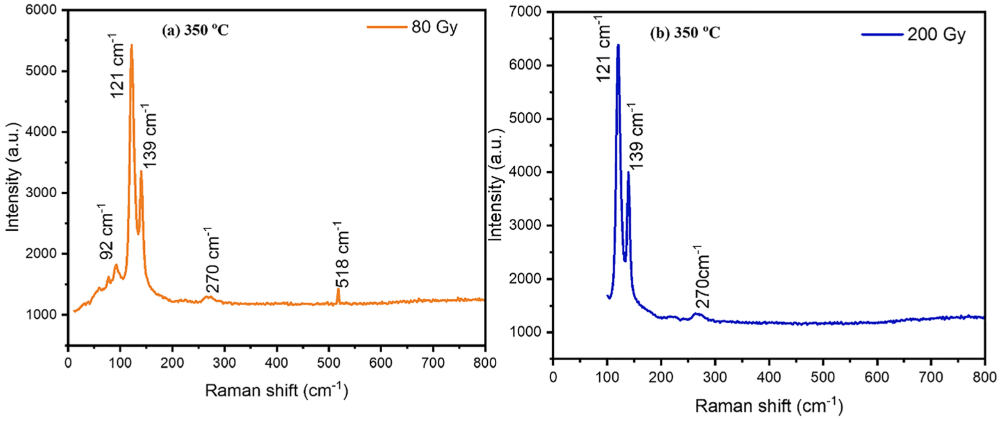

Fig. 6 Raman spectra of the 350 °C annealed sample for (a) 80 Gy and (b) 200 Gy dose irradiation.

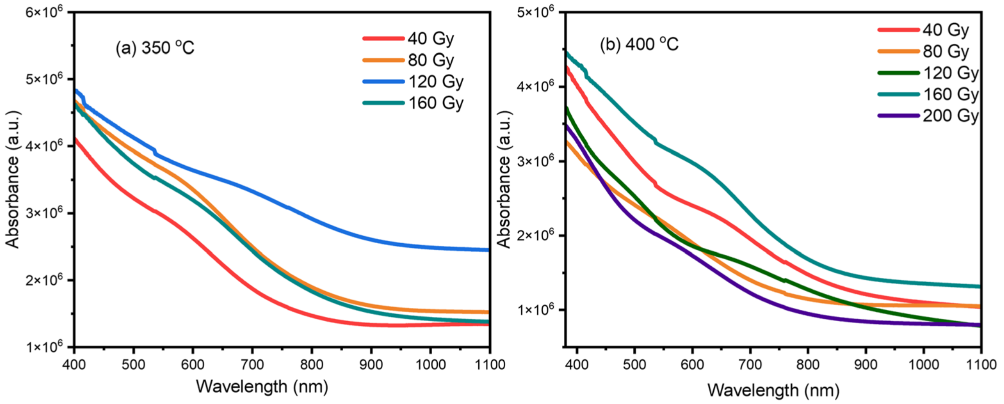

Fig. 7 UV visible spectroscopy absorbance spectra of both the (a) 350 °C and (b) 400 °C annealed samples at different gamma doses.

within the bandgap and increase free electron density. This shift moves the Fermi level closer to the conduction band (CB), partially filling the lowest energy states in the CB.[34] As a result, electrons in the valence band (VB) require additional energy to undergo transition to unoccupied higher-energy states in the CB. This increases the apparent optical band gap, as the energy difference between the highest occupied state in the VB and the lowest unoccupied state in the CB becomes larger. Thus, the band gap enhancement is attributed to the filling of low-energy CB states and the need for extra energy for VB electrons to transition into the CB.[24]

In the 350 °C annealed sample, the optical band gap decreased with increasing irradiation dose. This behaviour can be attributed to the introduction of additional energy levels

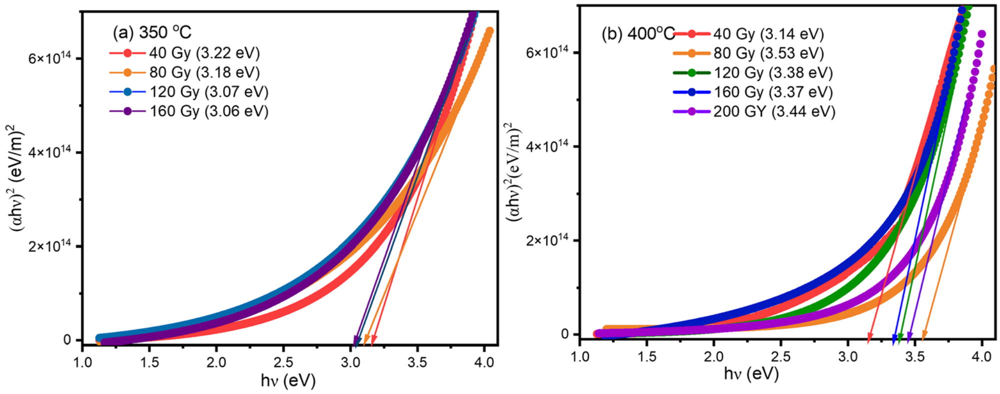

Fig. 8 Tauc plot of both annealed samples at (a) 350 °C and (b) 400 °C at different gamma doses for optical band gap measurement.

Table 5 Optical band gap value of the 350 °C and 400 °C annealed samples at different gamma doses

| | Optical band gap $\left(E_g^\circ\right)$ (eV) | |
|---|---|---|
| Dose value (Gy) | 350 °C | 400 °C |
| 40 | 3.22 | 3.14 |
| 80 | 3.18 | 3.53 |
| 120 | 3.07 | 3.38 |
| 160 | 3.06 | 3.37 |
| 200 | — | 3.44 |

within the forbidden gap, corresponding to various defect states induced by irradiation. The trend is also consistent with the XRD results, which show a reduction in crystallite size with increasing dose. Although a decrease in crystallite size typically causes a slight increase in band gap (in the meV range), the dominant effect of defect formation outweighs this contribution, leading to an overall reduction in band gap. Similarly, we observed greater absorption in the visible region for the irradiated sample, which was opposite to the observation at 400 °C. Tohidi *et al.*[35] reported the effect of gamma irradiation on the band gap where the band gap decreases with the increase in the dose of gamma irradiation due to the formation of defects. Hence, with the increase in dose, the disorder in the structure increases, which leads to a decrease in the band gap.[36]

**Photoluminescence study.** Photoluminescence analysis was one of the fundamental studies to understand the effect of irradiation on the defect state and its behaviour with the dose value. It could detect the presence of exciton fine structures, as well as impurities and defects, which typically impact the quality of materials.[37] Here, the excitation wavelength used was 350 nm to study the defect level intensity variation with dose value, hence the PL emissions don't include the peak related to near band edge emissions.

All the 400 °C irradiated samples show the dominating low-level defect emission peaks in the range of 600–750 nm (red emission) (Fig. 10(a)). The expected peaks were in the green emission range, which belongs to oxygen-related defects obtained for the non-irradiated sample.[20] This shift in peaks towards the lower energy side (red shift) for the irradiated sample indicates the formation of several mid band gap defects induced due to irradiation, since Gamma irradiation ($Co^{60}$ of 1.33 MeV) leads to the formation of probabilistically more favourable electron–hole pairs by Compton scattering and also the formation of lattice defects.[38] With irradiation dose (except for 40 Gy to 80 Gy), the intensity of the red emission peaks decreased. Memesa *et al.*[39] attributed this to a modification in surface defect density or due to low recombination rate. Jouini *et al.*[40] attributed the reduction to bond breaking around the luminescent atom and the formation of a low-level defect related to interstitial ions. Jin Wang *et al.*[41] reported that this decrement was due to non-radiative recombination. Defects such as vacancies and interstitial atomic substitutions act as dominant centres for non-radiative recombination, leading to the formation of mid-gap defect states that suppress radiative emission peaks. With an increase in irradiation dose from 40 Gy to 80 Gy, a clear disappearance of the green and yellow emission peaks (550–600 nm), associated with oxygen-related defects, is observed. These peaks were prominent in the non-irradiated sample.[42] The objective of correlating radiation-induced defects with optical behavior was met through optical absorption and photoluminescence studies, which demonstrated band gap narrowing and emission quenching due to defect-mediated non-radiative recombination.

A similar study was conducted for a 350 °C annealed sample at doses of 80 Gy and 200 Gy, as shown in Fig. 9. The results show a similar trend to the 400 °C annealed sample. Irrespective of crystallinity alteration for both sets of samples (350 °C and 400 °C), the effect of irradiation follows the reduction in radiative emission by non-radiative recombination.

### Electron paramagnetic resonance (EPR) spectral analysis

The nature and behaviour of defects under irradiation are analysed using EPR, where the *g*-factor value provides the electronic nature of the defects and defect intensity variation with irradiation, and also gives information about the surrounding environment near defects. EPR spectrometers commonly use a phase-sensitive detector that converts the raw absorption signal into its first derivative. Consequently, the EPR spectrum appears as the first derivative of the absorption

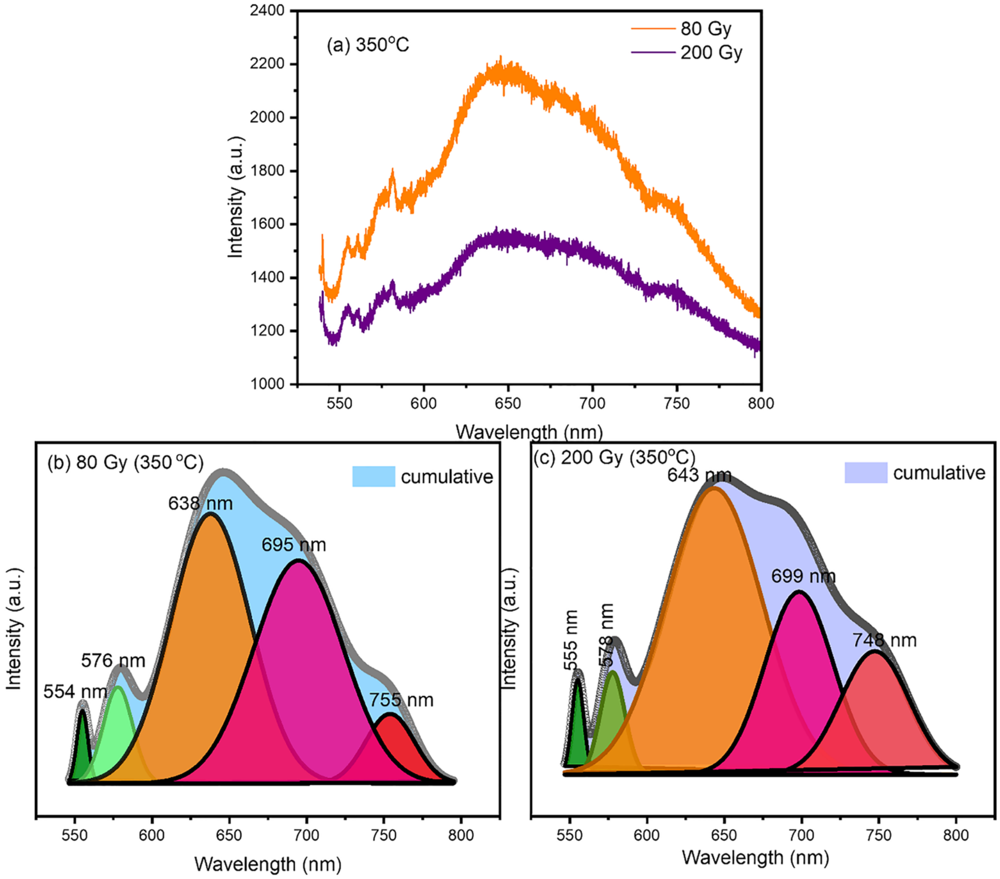

Fig. 9 The Pl analysis graphs of the 350 °C annealed sample: (a) raw data, (b) 80 Gy dose peak fitting and (c) 200 Gy dose peak fitting.

curve. The zero-crossing points in this derivative spectrum align with the peaks of the original absorption signal. These points are crucial for pinpointing the centre of the signal, allowing accurate identification of the resonance conditions and properties of the paramagnetic species being studied. At room temperature, X-band (9.25 GHz) measurements typically yield a differential peak that is broad in nature. As a result, peaks corresponding to different components of the *g*-tensor in anisotropic materials are difficult to resolve, and signals arising from different paramagnetic defect sites often overlap and merge into a single feature. Hence, a proper fitting technique is essential to resolve the different paramagnetic centres and to obtain their corresponding *g* tensor components. Easyspin is a dedicated software used to simulate the EPR signals of chemical composition and also least squares fit (LSF) the experimental data to obtain the *g* values.[43]

Bulk $TeO_2$ is inherently diamagnetic, so any EPR signal detected is likely due to defects involving oxygen or tellurium. Although elemental tellurium interstitials are also diamagnetic, ionised tellurium ($Te^{4+}$) is diamagnetic in nature. The possible paramagnetic defect was the $V_O^\bullet$ centre described as an oxygen vacancy trapped with a lone electron, resulting in the $S = 1/2$ (doublet) spin state, paramagnetic in nature.[44] A diamagnetic oxygen trap centre can exist, and after irradiation it may capture an electron released from the $V_O^\bullet$ center, forming a paramagnetic three-electron trap $V_O'$. Since the *g* values associated with oxygen vacancies are typically close to that of a free electron ($g_e = 2.0023$),[44–49] tellurium interstitials also cannot be excluded from consideration. While tellurium vacancies ($V_{Te}$) are generally EPR inactive, interstitial tellurium may exist in multiple oxidation states, such as neutral $Te^0$, singly ionized $Te^+$, or doubly ionized $Te^{2+}$. These interstitials act as donor centres, and due to the stronger spin–orbit coupling of heavier elements, they are associated with larger *g* values.[44,50]

The X-band EPR intensities of the films annealed at 350 °C and 400 °C before and after 200 Gy irradiation were compared, revealing a clear decrease in signal intensity after irradiation for the 350 °C film (see Fig. 11(a)). This reduction is consistent with a lower concentration of paramagnetic defect centres. Complementary XRD analysis indicates a decrease in overall crystallinity, while the appearance of new peaks at higher doses and their increased intensity point to finer crystallites and a stronger existing crystalline phase. Together, these features suggest that irradiation causes microstructural reorganisation and phase refinement that stabilises the lattice and reduces the number of EPR-active defect centres.[51,52] In the case of the 400 °C sample, there was an increase in the intensity of the EPR signal after irradiation (Fig. 11(b)). Conversely, XRD analysis shows an increase in crystallite size along with the intense peaks and new peaks were formed at higher irradiation doses.

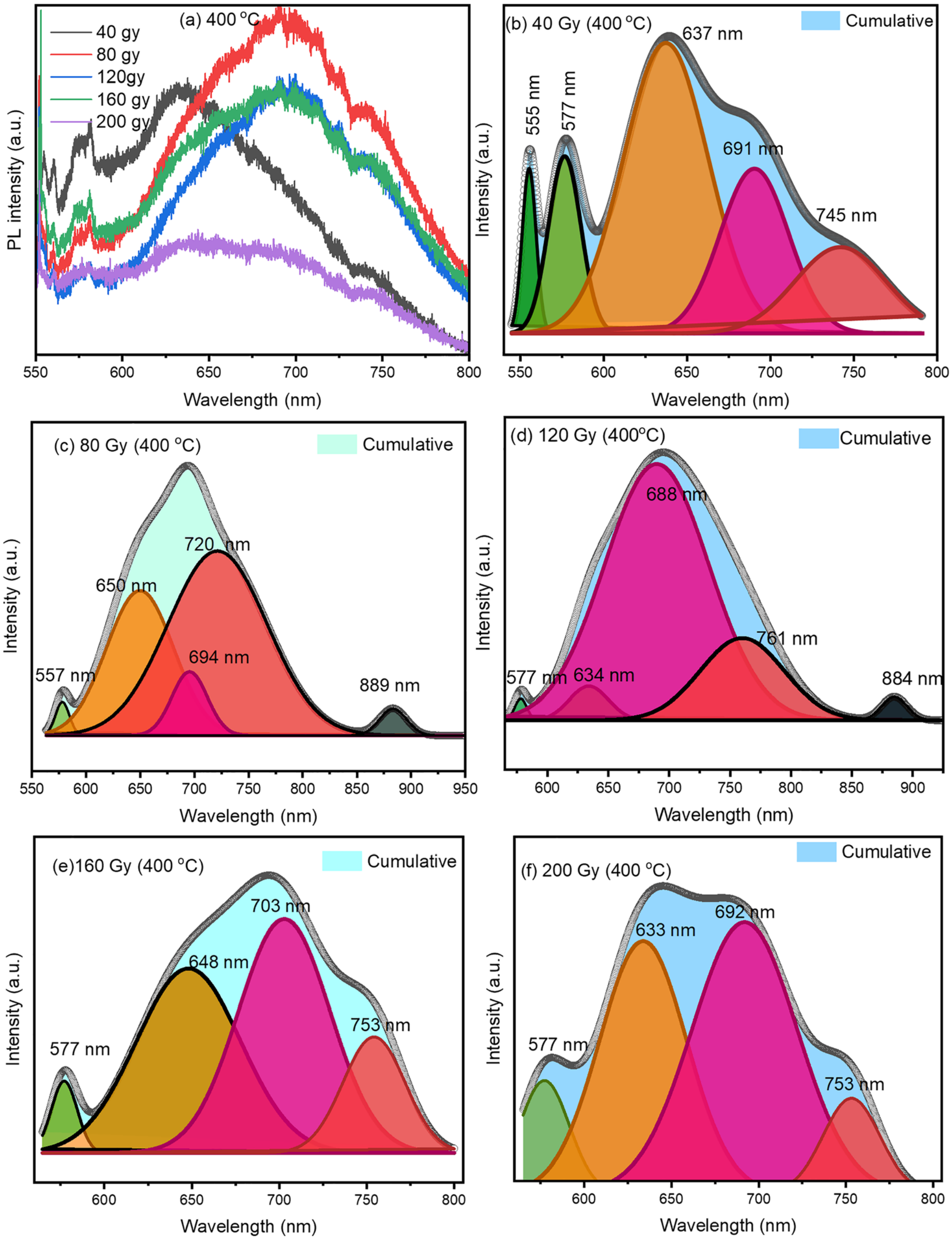

Fig. 10 PL spectra analysis graph of the 400 °C annealed sample: (a) raw spectra and peak fitting of (b) 40 Gy, (c) 80 Gy, (d) 120 Gy, (e)160 Gy, and (f) 200 Gy doses.

According to the existing studies, systems with a negative spin-coupling constant (hole-type centres) generally show *g*-factors higher than the free-electron *g*-value ($g_e$), causing their resonance signals to appear at lower magnetic fields. In contrast, electron-type centres typically exhibit *g*-factors lower than $g_e$, with their signals shifting to higher magnetic fields.[53] The obtained spectra show a broad signal, generally due to room temperature measurement, the raw data were fitted using Easyspin software in MATLAB. For the 350 °C unirradiated (0 Gy) sample, the EPR spectrum was best modelled by a three-spin system (Fig. 12(a)), each corresponding to distinct paramagnetic defect centres: oxygen vacancies with trapped electrons forming $F^+$ centres, hole centres near oxygen atoms or tellurium lattice sites, and tellurium ion-related defects (such as $Te^{2+}$). After irradiation with 200 Gy, however, the EPR signal could be accurately fitted using only a single spin system (Fig. 12(b)), indicating a reduction in the diversity of detectable paramagnetic defect centres. While gamma irradiation typically increases defect formation and concentration, in this case, it likely altered the nature of the defects, potentially generating EPR-inactive defect sites that do not contribute to the observable signal, and even PL data show the reduction in intensity of the photoactive

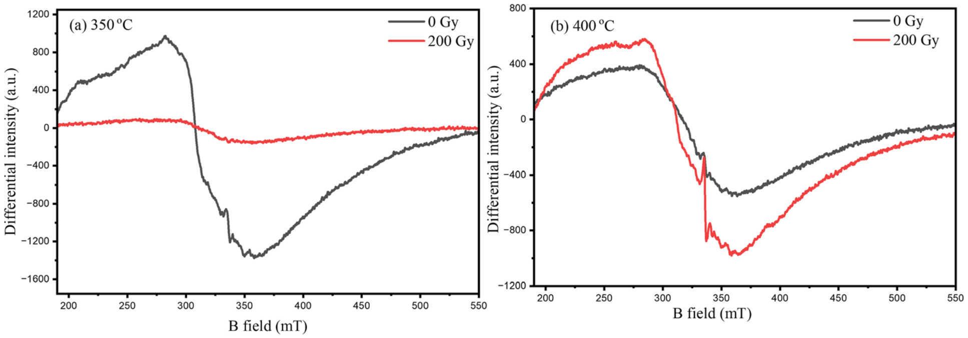

Fig. 11 EPR signal intensity comparison of (a) 350 °C and (b) 400 °C annealed samples before and after irradiation.

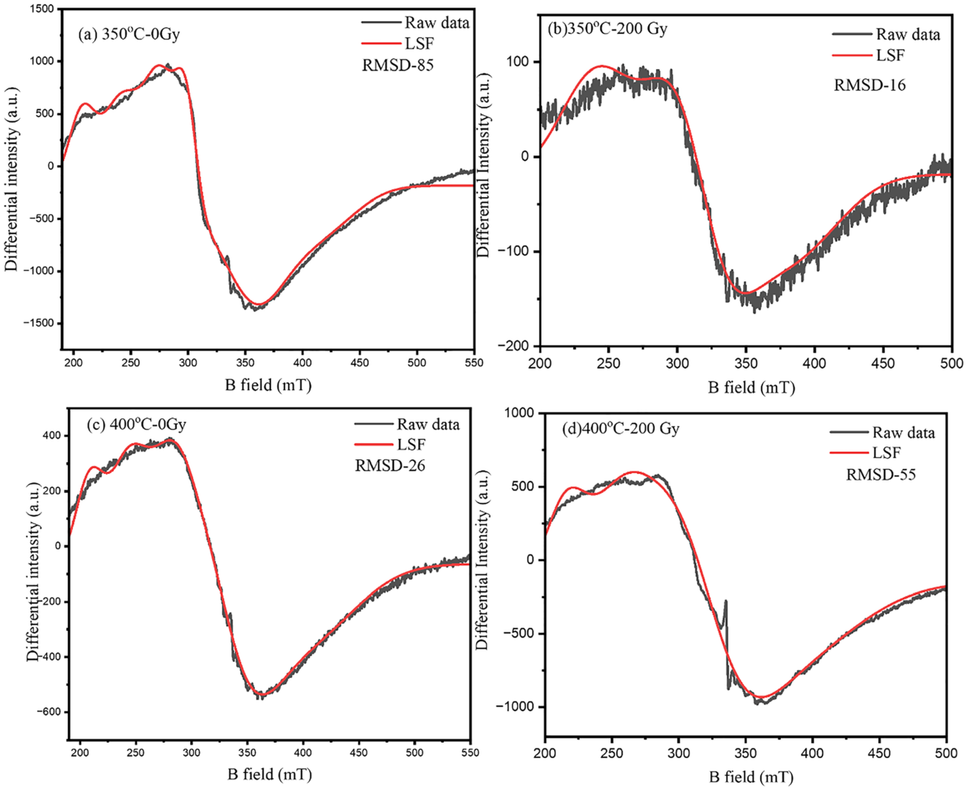

Fig. 12 EPR spectra of (a) 350 °C–0 Gy, (b) 350 °C–200 Gy, (c) 400 °C–0 Gy and (d) 400 °C–200 Gy samples showing variation of differential intensity *vs.* B field value along with LSF data.

defect sites after irradiation. The principal components of the *g* tensor, reported in Table 6, reflect the anisotropic crystal structure of $TeO_2$, with three distinct values arising from the anisotropic environment surrounding the defects. The broad EPR signal observed is attributed to the overlap of multiple defect centres' resonances. Among these, the larger *g* tensor component is associated with oxygen hole centres and tellurium ion-related defects, which exhibit anisotropic behaviour consistent with the crystal's structural arrangement. This explanation highlights that gamma irradiation not only affects defect concentration but can also modify defect characteristics and symmetry, leading to changes in EPR spectral features, including signal broadening and variations in the *g* tensor components.[51,54,55] Similarly, *g* values were obtained by LSF using Easyspin for the 400 °C–0 Gy sample, where proper fitting was reached using 3 spin systems (System 1, System 2 and System 3)

Table 6 *g* tensor components of spin systems for defect states in the 350 °C and 400 °C samples before and after (200 Gy) irradiation, obtained using fitting in Easyspin software

| | | 0 Gy | | | 200 Gy | | |
|---|---|---|---|---|---|---|---|
| Sample name | | $g_1$ | $g_2$ | $g_3$ | $g_1$ | $g_2$ | $g_3$ |
| 350 °C | System 1 | 1.56 | 2.38 | 3.29 | 1.74 | 2.13 | 2.84 |
| | System 2 | 1.66 | 2.14 | 2.80 | — | — | — |
| | System 3 | 1.90 | 2.24 | 2.09 | — | — | — |
| 400 °C | System 1 | 1.60 | 2.80 | 3.24 | 1.75 | 2.02 | 3.12 |
| | System 2 | 1.70 | 1.82 | 2.13 | 1.60 | 2.13 | 2.64 |
| | System 3 | 1.95 | 2.02 | 2.77 | — | — | — |

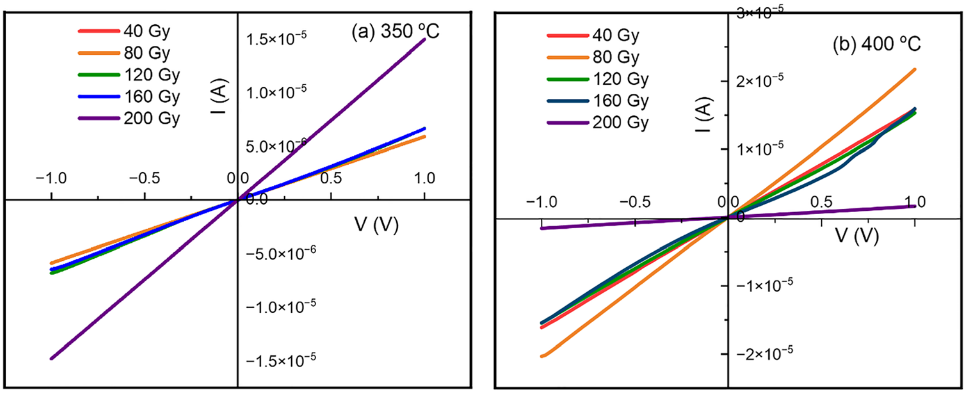

Fig. 13 *I–V* characteristics of (a) 350 °C and (b) 400 °C annealed samples for different gamma doses.

shown in Fig. 12(c) and (d), and their respective *g* components were mentioned in the table. Here, the presence of paramagnetic defect centres corresponds to the various defect centres observed in the 350 °C, 0 Gy sample. After irradiation (at 200 Gy), the sample fitted with two spin systems corresponds to 2 different paramagnetic defect centres (see Table 6). The evolution of paramagnetic defects with irradiation dose, a key objective of the study, was clearly established through EPR analysis, showing systematic modulation of signal intensity.

## Electrical studies

Electrical studies were conducted to obtain the electrical parameters of each set of samples at different irradiation doses using the Van der Pauw Hall measurement, including current–voltage (*I–V*) characteristics. *I–V* characteristics show a different trend for both the 350 °C and 400 °C samples (Fig. 13(a) and (b)).

Table 7 Electrical properties of the annealed sample at different gamma doses, which include mobility, resistivity and carrier density, obtained using the Van der Pauw Hall method

| | | Dose value | | | | |
|---|---|---|---|---|---|---|
| Sample | Parameter | 40 Gy | 80 Gy | 120 Gy | 160 Gy | 200 Gy |
| 350 °C | $n$ ($10^6$) (cm$^{-3}$) | 13.5 | 72.1 | 50.1 | 39.8 | 4.7 |
| | $\mu$ (cm$^2$ V$^{-1}$ s$^{-1}$) | 17.3 | 5.5 | 14.9 | 9.2 | 152.0 |
| | $\rho$ (Ω cm) | 2.7 | 1.6 | 0.8 | 1.7 | 0.9 |
| 400 °C | $n$ ($10^6$) (cm$^{-3}$) | 30.0 | 28.1 | 10.0 | 3.8 | 0.3 |
| | $\mu$ (cm$^2$ V$^{-1}$ s$^{-1}$) | 6.4 | 25.8 | 63.2 | 10.4 | 18.5 |
| | $\rho$ (Ω cm) | 3.3 | 0.9 | 1.0 | 1.6 | 111.6 |

For the 350 °C sample, *I–V* characteristics show a small increase in slope value with the dose value up to 160 Gy and a greater increase in slope value for 200 Gy. For the 400 °C annealed sample, the slope value reduced for 200 Gy, showing a greater increase in resistivity. The increase in electric current value at high dose for the 350 °C annealed sample, despite lower crystallinity, can be linked to a significant rise in carrier mobility. Even Hall measurement shows the increment in mobility at a higher dose (200 Gy)[56] (Table 7). With an increase in disorder in the films, irradiation can introduce localised states and defects that enhance hopping conduction, sometimes leading to a dramatic increase in mobility for certain dose ranges.[57–59]

The reduction in current and significant increase in resistivity at high gamma irradiation doses for a 400 °C annealed sample indicate that, in highly crystalline films, excessive irradiation causes the buildup of defects that serve as recombination centres or traps. EPR studies revealed the presence of different paramagnetic defect sites in the 400 °C and 200 Gy irradiated samples. These defects reduce both carrier concentration and mobility. Proper EPR peak fitting was obtained by considering two spin systems, which represent two different paramagnetic defect centres responsible for the reduction in conductivity. These defects lower both carrier concentration and mobility, leading to an increase in resistance. The 350 °C and 400 °C annealed samples show contrasting behaviour even in electrical studies, which was consistent with the other studies, such as structural and chemical.

Table 8 presents the values of various parameters compared with the present study at different dose ranges. Each oxide thin

Table 8 Summary of electrical, optical and structural parameters of reported studies on gamma-irradiated oxide thin films at different dose ranges

| Thin film material | Dose range (Gy) | Band gap (eV) | Mobility (cm$^2$ V$^{-1}$ s$^{-1}$) | Resistivity (Ω cm) | Grain size (nm) | Ref. |
|---|---|---|---|---|---|---|
| $SnO_2$ | 0–200k | 3.80–3.48 | 3.43–6.71 | 0.0067–0.0012 | 261–536 | Rashmi Kajal *et al.*[60] |
| $In_2O_3$ | 0–100k | 3.45–3.3 | 1.17–7.18 | 65.02–1.40 | 80.57–69.87 | Nefzi *et al.*[61] |
| F-doped $In_2O_3$ | 1k–100k | 3.32–3.45 | 6.60–14.00 | 0.14–0.27 | 76.0–79.0 | Nefzi *et al.*[62] |
| $SnO_2$ | 0–90k | 4.01–3.95 | — | — | 39.10–40.10 | S. Chayoukhi *et al.*[63] |
| $MoO_3$ | 0–90k | 3.92–3.96 | — | — | 105–104 | F. Chandoul *et al.*[64] |
| $In_2O_3$ | 25–200 | — | 7.80–75.4 | 0.19–0.04 | 32.50–36.30 | C Aparna *et al.*[65] |
| W-doped $In_2O_3$ | 25–200 | 3.78–3.66 | 8.36–21.88 | 0.03–0.12 | 17.98–21.87 | C Aparna *et al.*[66] |
| $TeO_2$ (350 °C) | 40–200 | — | 17.3–152.0 | 2.7–0.9 | 33.20–27.50 | Present work |
| $TeO_2$ (400 °C) | 40–200 | 3.14–3.44 | 6.4–18.5 | 3.3–111.6 | 42.10–50.00 | |

film exhibits a distinct response to gamma irradiation. The physical parameters listed in the table vary with the irradiation dose; some studies report an increase in these properties with dose, while others observe a decrease. This suggests that the variations in electrical, optical, and structural properties with irradiation dose depend not only on the film material but also on factors such as the dose range, deposition conditions, and type of doping element. The present work showed a large change in electrical mobility (3.3 $cm^2 V^{-1} s^{-1}$–111.6 $cm^2 V^{-1} s^{-1}$) (400 °C) and electrical resistivity (3.3 Ω cm–111.6 Ω cm) (350 °C) for doses up to 200 Gy.

## Conclusions

XRD analysis reveals that gamma irradiation significantly influences the effect of annealing temperature on β-$TeO_2$ thin films. At an annealing temperature of 350 °C, increasing the gamma dose leads to a reduction in crystallite size, accompanied by an increase in microstrain and dislocation density. This indicates increased defects and decreased crystallinity due to radiation damage. Conversely, for the 400 °C sample, irradiation led to an increase in crystallite size, suggesting that irradiation promotes crystal growth at this higher annealing temperature.

Morphological and chemical analyses confirmed oxygen loss and defect formation, directly linking thermal treatment to radiation-induced structural stability. Raman spectroscopy further substantiated these findings by evidencing lattice distortion or amorphization consistent with the XRD results. At 400 °C, irradiation leads to noticeable surface roughening and a reduction in oxygen composition. XPS analysis of the O 1s peak reveals the presence of oxygen vacancies in the 400 °C annealed sample after gamma irradiation. Raman spectra of the sample annealed at 400° show the Raman peak at a higher Raman shift. Conversely, higher-order peaks were absent at 350 °C after irradiation, which correlates with the other structural analysis. UV-vis study revealed a decrease in band gap with dose value for the sample annealed at 350 °C, but an increase was observed at 400 °C. The intensity of the EPR signal increased in the case of the 400 °C annealed sample at 200 Gy, confirming the formation of paramagnetic defects like oxygen vacancies. *I–V* analysis shows that the sample annealed at 400 °C exhibited a sudden increase in resistivity at 200 Gy. The study concludes that although both samples exhibited the same crystal phase (β-$TeO_2$), irradiation affected them differently. Photoluminescence (PL) analysis revealed a linear variation in defect peak intensity with increasing dose for both sample sets. Collectively, these results achieve the objective of establishing a unified defect–structure–property relationship and demonstrate the feasibility of engineering $TeO_2$ thin films as tunable EPR-based gamma dosimeters for precise radiation-sensing applications.

## Conflicts of interest

The authors declare that they have no known competing financial interests or personal relationships that could have appeared to influence the work reported in this paper.

## Data availability

The authors confirm that the data supporting the findings of this study are available within the article.

## References

1 M. Elsafi, M. I. Sayyed and T. A. Hanafy, Experimental study of different oxides in $B_2O_3$–ZnO–BaO glass system for gamma-ray shielding, *Sci. Rep.*, 2025, **15**(1), 2618.

2 R. K. Guntu, Raman deconvolution, photoluminescence, thermoluminescence, radiation shielding and dielectric investigations of $Cu^{2+}$: $Li_2Al_2SiO_6$ glasses for Optoelectronic use, *Ceram. Interfaces*, 2025, **51**(12), 16524–16538.

3 R. K. Guntu, P. Ashok, K. Sivaram, P. B. Shetty, S. Babu and M. Israr, Investigations on thermoluminescence, photoluminescence and radiation shielding properties of $Dy_2O_3$ doped $Li_2O$-$Al_2O_3$-$SiO_2$-$Y_2O_3$ glasses for thermoluminescent dosimeter applications, *Appl. Phys. A: Mater. Sci. Process.*, 2025, **131**(9), 701.

4 J. Budida, C. S. Rao, N. R. Chand and R. K. Guntu, Spectral and Structural Tailoring of $Sm_2O_3$-Doped LiF-$La_2O_3$-PbO-$B_2O_3$ Glasses for Advanced Luminescent Devices, *J. Electron. Mater.*, 2025, **54**(11), 10611–10647.

5 J. Budida, C. S. Rao, N. R. Chand, R. K. Guntu and N. K. Mohan, Multifunctional $Pr_2O_3$ doped lithium fluoro lanthanum oxy lead borate glasses for advanced photonic and radiation shielding applications, *J. Alloys Compd.*, 2025, 1037.

6 J. Thumma and R. K. Guntu, Design and evaluation of TiO2-enhanced phosphate glasses for dual-functionality: Photonic applications and radiation safety, *Phys. B*, 2025, 716.

7 M. J. Sumalatha, R. K. Guntu, K. Sivaram and P. B. Shetty, A holistic approach to $Cr_2O_3$-doped lithium lead borosilicate glasses: probing thermal stability, optical emissions, and gamma shielding, *J. Non-Cryst. Solids*, 2025, 666.

8 N. Dewan, K. Sreenivas and V. Gupta, Comparative study on TeO2 and TeO3 thin film for γ-ray sensor application, *Sens. Actuators, A*, 2008, **147**(1), 115–120.

9 M. Mohil and G. Anil Kumar, Gamma Radiation Induced Effects in $TeO_2$ Thin Films, *J. Nano- Electron. Phys.*, 2013, **5**, 02018.

10 V. L. Deringer, R. P. Stoffel and R. Dronskowski, Thermochemical Ranking and Dynamic Stability of TeO 2 Polymorphs from *Ab Initio* Theory, *Cryst. Growth Des.*, 2014, **14**(2), 871–878. Available from: https://pubs.acs.org/doi/10.1021/cg401822g.

11 A. Zavabeti, P. Aukarasereenont, H. Tuohey, N. Syed, A. Jannat and A. Elbourne, *et al.*, High-mobility p-type semiconducting two-dimensional β-TeO2, *Nat. Electron.*, 2021, **4**(4), 277–283. Available from: https://www.nature.com/articles/s41928-021-00561-5.

12 P. Jeya, L. Kungumadevi, S. K. Binu, A. Jayakumar and A. Kandasami, Exploring the transformation: High-dosage gamma irradiation's role in tuning structural, optical, and

electrical properties of cadmium-doped lead sulfide (PbS) nanoparticles, *Chem. Phys. Impact*, 2024, 8.

13 S. K. Thatikonda, A. Kandasami, S. Rabha, D. Pamu and A. K. Nirala, Enhancement of crystallinity and the optical properties in gamma irradiated and thermally annealed cobalt doped MgTiO3 thin films, *Thin Solid Films*, 2024, 804.

14 R. Lok, M. U. Doğan, S. Kaya, U. Soykan and C. Terzioğlu, Gamma radiation-induced modifications in structural, optical, and electrical characteristics of p-NiO/n-Si heterojunction diodes, *Radiat. Phys. Chem.*, 2025, 229.

15 G. P. Summers, E. A. Burke, P. Shapiro, S. R. Messenger and R. J. Walters, Damage correlations in semiconductors exposed to gamma, electron and proton radiations, *IEEE Trans. Nucl. Sci.*, 1993, **40**(6), 1372–1379.

16 S. Kaya, S. Abubakar and E. Yilmaz, Co-60 gamma irradiation influences on device characteristics of n-SnO 2/p-Si heterojunction diodes, *Nucl. Instrum. Methods Phys. Res., Sect. B*, 2019, **445**, 63–68.

17 B. Oryema, E. Jurua, I. G. Madiba, M. Nkosi, J. Sackey and M. Maaza, Effects of low-dose γ-irradiation on the structural, morphological, and optical properties of fluorine-doped tin oxide thin films, *Radiat. Phys. Chem.*, 2020, 176.

18 R. Kajal, B. R. Kataria, K. Asokan and D. Mohan, Effects of gamma radiation on structural, optical, and electrical properties of SnO2 thin films, *Appl. Surf. Sci. Adv.*, 2023, **15**, 100406.

19 C. Zhao, Y. Yang, L. Luo, S. Shao, Y. Zhou and Y. Shao, *et al.*, γ-ray induced formation of oxygen vacancies and Ti3+ defects in anatase TiO2 for efficient photocatalytic organic pollutant degradation, *Sci. Total Environ.*, 2020, **747**, 141533.

20 K. Chandra, M. G. Mahesha and P. K. Shetty, Annealing-induced phase transformation in vapor deposited tellurium dioxide thin films and its structural, chemical analysis, *Mater. Chem. Phys.*, 2025, 330.

21 R. Schlögl and H. P. Boehm, Influence of crystalline perfection and surface species on the X-ray photoelectron spectra of natural and synthetic graphites, *Carbon*, 1983, **21**(4), 345–358. Available from: https://linkinghub.elsevier.com/retrieve/pii/0008622383901276.

22 G. Lakshminarayana, S. O. Baki, A. Lira, M. I. Sayyed, I. V. Kityk and M. K. Halimah, *et al.*, X-ray photoelectron spectroscopy (XPS) and radiation shielding parameters investigations for zinc molybdenum borotellurite glasses containing different network modifiers, *J. Mater. Sci.*, 2017, **52**(12), 7394–7414.

23 H. Y. Lee, B. K. Wu and M. Y. Chern, Study on the formation of zinc peroxide on zinc oxide with hydrogen peroxide treatment using x-ray photoelectron spectroscopy (XPS), *Electron. Mater. Lett.*, 2014, **10**(1), 51–55.

24 A. K. Anbalagan, S. Gupta, A. Kumar, S. C. Haw, S. S. Kulkarni and N. H. Tai, *et al.*, Gamma Ray Irradiation Enhances the Linkage of Cotton Fabrics Coated with ZnO Nanoparticles, *ACS Omega*, 2020, **5**(25), 15129–15135.

25 M. A. K. Purbayanto, A. Rusydi and Y. Darma, The effect of crystallinity on the surface modification and optical properties of ZnO thin films, *Phys. Chem. Chem. Phys.*, 2020, **22**(4), 2010–2018.

26 A. Sahai and N. Goswami, Probing the dominance of interstitial oxygen defects in ZnO nanoparticles through structural and optical characterizations, *Ceram. Interfaces*, 2014, **40**(9), 14569–14578. Available from: https://linkinghub.elsevier.com/retrieve/pii/S0272884214009353.

27 G. Greczynski and L. Hultman, X-ray photoelectron spectroscopy: Towards reliable binding energy referencing, *Prog. Mater. Sci.*, 2020, **107**, 100591. Available from: https://linkinghub.elsevier.com/retrieve/pii/S0079642519300738.

28 H. Estrade-Szwarckopf, XPS photoemission in carbonaceous materials: A ''defect'' peak beside the graphitic asymmetric peak, *Carbon*, 2004, **42**(8–9), 1713–1721. Available from: https://linkinghub.elsevier.com/retrieve/pii/S0008622304001629.

29 A. P. Mirgorodsky, T. Merle-Méjean, J. C. Champarnaud, P. Thomas and B. Frit, Dynamics and structure of TeO2 polymorphs: model treatment of paratellurite and tellurite; Raman scattering evidence for new γ- and δ-phases, *J. Phys. Chem. Solids*, 2000, **61**(4), 501–509. Available from: https://linkinghub.elsevier.com/retrieve/pii/S0022369799002632.

30 J. C. Champarnaud-Mesjard, S. Blanchandin, P. Thomas, A. Mirgorodsky, T. Merle-Méjean and B. Frit, Crystal structure, Raman spectrum and lattice dynamics of a new metastable form of tellurium dioxide: γ-TeO2, *J. Phys. Chem. Solids*, 2000, **61**(9), 1499–1507. Available from: https://linkinghub.elsevier.com/retrieve/pii/S0022369700000123.

31 M. Ceriotti, F. Pietrucci and M. Bernasconi, Ab initio study of the vibrational properties of crystalline TeO2: The:alpha, Beta, and gamma phases, *Phys. Rev. B: Condens. Matter Mater. Phys.*, 2006, **73**(10), 104304. Available from: https://link.aps.org/doi/10.1103/PhysRevB.73.104304.

32 A. P. Mirgorodsky, T. Merle-Méjean, J. C. Champarnaud, P. Thomas and B. Frit, Dynamics and structure of TeO 2 polymorphs: model treatment of paratellurite and tellurite; Raman scattering evidence for new g- and d-phases, *J. Phys. Chem. Solids*, 2000, **61**, 501–509. Available from: https://www.elsevier.nl/locate/jpcs.

33 S. Aldawood and S. Mansoor Ali, Effects of gamma irradiation on the properties of $Ce_2S_3$ thin films, *J. King Saud Univ., Sci.*, 2024, **36**(2), 103075.

34 J. S. Bhat, A. S. Patil, N. Swami, B. G. Mulimani, B. R. Gayathri and N. G. Deshpande, *et al.*, Electron irradiation effects on electrical and optical properties of sol–gel prepared ZnO films, *J. Appl. Phys.*, 2010, 043513.

35 T. Tohidi, N. Yousefpour Novini and K. Jamshidi-Galeh, Effect of Gamma irradiation on optical characteristics of Fe-doped CdS thin films prepared using chemical bath deposition, *Opt. Mater.*, 2024, 151.

36 S. Joseph and O. N. Balasundaram, Effect of gamma radiation on structural, optical and electrical properties of ZnO thin films, *Optoelectron. Adv. Mater., Rapid Commun.*, 2017, **11**, 377–380.

37 V. Chauhan, D. Gupta, N. Koratkar and R. Kumar, Phase transformation and enhanced blue photoluminescence of zirconium oxide poly-crystalline thin film induced by Ni ion beam irradiation, *Sci. Rep.*, 2021, **11**(1), 17672.

38 K. Ahn, Y. K. Ooi, F. Mirkhosravi, J. Gallagher, A. Lintereur and D. Feezell, *et al.*, Differences in electrical responses and recovery of GaN p + n diodes on sapphire and freestanding GaN subjected to high dose $^{60}$Co gamma-ray irradiation, *J. Appl. Phys.*, 2021, **129**(24), 245703.

39 M. Memesa, S. Lenz, S. G. J. Emmerling, S. Nett, J. Perlich and P. Müller-Buschbaum, *et al.*, Morphology and photoluminescence study of titania nanoparticles, *Colloid Polym. Sci.*, 2011, **289**(8), 943–953.

40 K. Jouini, A. Raouafi, W. Dridi, M. Daoudi, B. Mustapha and R. Chtourou, *et al.*, Investigation of gamma-ray irradiation induced phase change from NiO to $Ni_2O_3$ for enhancing photocatalytic performance, *Optik*, 2019, 195.

41 J. Wang, X. Yue, J. Q. Zhu, L. Hu, R. Liu and C. Cong, *et al.*, Revealing the origin of PL evolution of InSe flake induced by laser irradiation, *RSC Adv.*, 2023, **13**(12), 7780–7788.

42 Investigation of Oxygen Vacancy and Interstitial Oxygen Defects in ZnO Films by Photoluminescence and X-Ray Photoelectron Spectroscopy [Internet]. Available from: https://iopscience.iop.org/0256-307X/24/7/089.

43 https://www.easyspin.org/[Internet]. [cited 2025 Oct 17]. Easyspin https://www.easyspin.org/. Available from: https://www.easyspin.org/.

44 L. A. Kappers, O. R. Gilliam, R. H. Bartram, A. Watterich and I. Földvári, Discovery of a self-trapped-electron center in α-TeO2, *Radiat. Eff. Defects Solids*, 2002, **157**(6–12), 671–676.

45 Metal oxide catalysis, 2 volume set. Wiley; 2009.

46 O. Al-Madanat, B. N. Nunes, Y. Alsalka, A. Hakki, M. Curti and A. O. T. Patrocinio, *et al.*, Application of EPR spectroscopy in TiO2 and $Nb_2O_5$ photocatalysis, *Catalysts*, 2021, **11**, 1514.

47 S. Aldawood and S. Mansoor Ali, Effects of gamma irradiation on the properties of $Ce_2S_3$ thin films, *J. King Saud Univ., Sci.*, 2024, **36**(2), 103075.

48 K. Hayashi, Y. Matsumura, S. Kobayashi, H. Morishita, H. Koike and S. Miwa, *et al.*, Electron paramagnetic resonance study of MgO thin-film grown on silicon, *J. Appl. Phys.*, 2017, **121**(21), 213901.

49 Y. Kutin, N. Cox, W. Lubitz, A. Schnegg and O. Rüdiger, In situ EPR characterization of a cobalt oxide water oxidation catalyst at neutral pH, *Catalysts*, 2019, **9**(11), 926.

50 K. Rakshyit, A. Wattericht, R. Gilliamf, L. A. Kapperst and G. J. Edwards, Electron spin resonance of Fe 3+ centres in alpha-TeO 2:Fe Electron spin resonance of Fe3+ centres in a-TeOa:Fe, *J. Phys.: Condens. Matter.*, 1995, **7**, 2889–2899. Available from: https://iopscience.iop.org/0953-8984/7/14/025.

51 S. K. Misra, S. I. Andronenko, D. Tipikin, J. H. Freed, V. Somani and O. Prakash, Study of paramagnetic defect centers in as-grown and annealed TiO2 anatase and rutile nanoparticles by a variableerature X-band and high-frequency (236 GHz) EPR, *J. Magn. Magn. Mater.*, 2016, **401**, 495–505.

52 E. Giamello, M. Chiesa and M. C. Paganini, Point defects in electron paramagnetic resonance, *Defects at oxide surfaces*, Springer International Publishing, Cham, 2015, pp. 303–326.

53 A. Antuzevics, A. Zarins, J. Cirulis, A. Fedotovs, A. Ansone and M. Rzepna, *et al.*, Hyperfine interactions of paramagnetic radiation-induced defect centres in advanced ceramic breeder pebbles, *Nucl. Mater. Energy*, 2024, **40**, 101698. Available from: https://linkinghub.elsevier.com/retrieve/pii/S2352179124001212.

54 H. Qin, X. Chen, J. Zhang, Y. Song, L. Zhang and Q. Liu, *et al.*, Electronic paramagnetic resonance analysis of point defects in lithium niobate: progress and prospects, *Mater. Adv.*, 2025, 6. 6648–6663.

55 J. M. Giehl, W. M. Pontuschka, L. C. Barbosa and Z. M. C. Ludwig, EPR of γ-induced paramagnetic centers in tellurite glasses, *J. Non-Cryst. Solids*, 2010, **356**(35–36), 1762–1767.

56 G. A. Mohi, S. M. Kadhim and H. H. Abdullah, Annealing temperature effect on TeO2 thin films for optical detection devices, *Int. J. Nanoelectron. Mater.*, 2023, **16**, 313–324.

57 K. Arshak and O. Korostynska, Preliminary studies of properties of oxide thin/thick films for gamma radiation dosimetry, *Mater. Sci. Eng., B*, 2004, **107**(2), 224–232. Available from: https://linkinghub.elsevier.com/retrieve/pii/S0921510703006482.

58 K. Arshak and O. Korostynska, Gamma Radiation Dosimetry Using Tellurium Dioxide Thin Film Structures, *Sensors*, 2002, **2**, 347–355. Available from: https://www.mdpi.net/sensors.

59 K. Arshak and O. Korostynska, Response of metal oxide thin film structures to radiation, *Mater. Sci. Eng., B*, 2006, **133**(1–3), 1–7. Available from: https://linkinghub.elsevier.com/retrieve/pii/S0921510706003060.

60 R. Kajal, B. R. Kataria, K. Asokan and D. Mohan, Effects of gamma radiation on structural, optical, and electrical properties of SnO2 thin films, *Appl. Surf. Sci. Adv.*, 2023, 15.

61 C. Nefzi, M. Souli, N. Beji, A. Mejri and N. Kamoun-Turki, Enhancement by high gamma radiations of optical and electrical properties of indium oxide thin films for solar devices, *J. Mater. Sci.*, 2017, **52**(1), 336–345.

62 C. Nefzi, M. Souli, N. Beji, A. Mejri and N. Kamoun-Turki, Improvement of structural, optical and electrical properties of iron doped indium oxide thin films by high gamma radiations for photocatalysis applications, *Mater. Sci. Semicond. Process.*, 2019, **90**, 32–40.

63 S. Chayoukhi, B. Gassoumi, H. Dhiflaoui, A. Mejri, A. Boukhachem and M. Amlouk, Effects of $^{60}$Co γ-radiation on the structural, morphological, optical, tribological and mechanical properties of SnO2 sprayed thin films, *Inorg. Chem. Commun.*, 2023, **155**, 111037. Available from: https://linkinghub.elsevier.com/retrieve/pii/S1387700323006494.

64 F. Chandoul, A. Boukhachem, F. Hosni, H. Moussa, M. S. Fayache and M. Amlouk, *et al.*, Change of the properties of nanostructured MoO3 thin films using gamma-ray irradiation, *Ceram. Int.*, 2018, **44**(11), 12483–12490.

65 C. Aparna, P. K. Shetty, M. G. Mahesha, N. Karunakara and I. Yashodhara, Structural, optical and sensitivity study of optimized indium oxide thin film for gamma sensing applications, *Sens. Actuators, A*, 2022, 345.

66 C. Aparna, M. G. Mahesha, N. Karunakara, I. Yashodhara and P. K. Shetty, Enhancement of gamma radiation sensitivity in tungsten-doped indium oxide thin films, *J. Lumin.*, 2025, 286.